frontiers in Earth Science

ORIGINAL RESEARCH
published: 14 February 2022
doi: 10.3389/feart.2021.813925

Characterization of the Full-Sized Pore Structure and Controlling Factors of the Coal-Bearing Shale in the Wuxiang Block, South-Central Qinshui Basin, China

Xueqing Zhang[1,2], *Xianqing Li*[1,2]*, *Jingwei Yang*[1,2], *Boxiang Zhang*[1,2], *Jian Sun*[3] and *Zhenfeng Yu*[4]

[1]State Key Laboratory of Coal Resources and Safe Mining, China University of Mining and Technology (Beijing), Beijing, China, [2]College of Geosciences and Surveying Engineering, China University of Mining Technology (Beijing), Beijing, China, [3]School of Energy Resources, China University of Geosciences (Beijing), Beijing, China, [4]Lanyan Coalbed Methane Engineering Research Co., Ltd., Shanxi Gas Group, Jincheng, China

OPEN ACCESS

Edited by:
Rui Liu,
Southwest Petroleum University, China

Reviewed by:
Qiming Huang,
Shandong University of Science and Technology, China
Zhentao Li,
Guangzhou Institute of Geochemistry (CAS), China
Wei Dang,
Xi'an Shiyou University, China

***Correspondence:**
Xianqing Li
Lixq@cumtb.edu.cn

Specialty section:
This article was submitted to Economic Geology, a section of the journal Frontiers in Earth Science

Received: 12 November 2021
Accepted: 21 December 2021
Published: 14 February 2022

Citation:
Zhang X, Li X, Yang J, Zhang B, Sun J and Yu Z (2022) Characterization of the Full-Sized Pore Structure and Controlling Factors of the Coal-Bearing Shale in the Wuxiang Block, South-Central Qinshui Basin, China. Front. Earth Sci. 9:813925. doi: 10.3389/feart.2021.813925

The characterization of the full-sized pore structure is important for the evaluation and prediction of the reservoir of shale gas with strong heterogeneity. It is of great scientific significance to explore the pore structure characteristics of overmature coal-bearing shale. Core descriptions, X-ray diffraction (XRD), vitrinite reflectance (*Ro*), field emission scanning electron microscopy (FE-SEM), high-pressure mercury intrusion porosimetry (MIP), and low-pressure N_2/CO_2 gas adsorption (N_2-/CO_2-GA) experiments were performed on overmature coal-bearing shale samples from the Wuxiang block, south-central Qinshui Basin, China. The results show that the total organic carbon (TOC) ranged from 0.29 to 8.36%, with an average of 3.84%, and the organic matter (OM) is dominated by type III kerogen. The minerals in the shale primarily consist of clay (43–85.5%, averaging 52.1%) and quartz (12.6–61.2%, averaging 43.5%). The major clay minerals are illite-smectite (I/S) and illite, ranging from 22.5 to 55.6% (mean 41.4%) and 8.7–52.7% (mean 32%), respectively. FE-SEM images reveal that intraparticle pores (IntraP pores) and interparticle pores (InterP pores) are widely developed in clay minerals, and organic pores are occasionally present. Mesopores make the greatest contribution to the total pore volume (PV), and micropores are the major contributors to the specific surface area (SSA). Clays are the main controllers of micropore development. Mesopores developed in the clay mineral layers are promoted by I/S but inhibited by illite. Macropores and microfractures are mainly developed in clays and quartz and do not correlate significantly with the TOC, or mineral composition, due to the influence of compaction and cementation. The TOC and minerals affect pore structure characteristics mainly by influencing micropores.

Keywords: characterization, coal-bearing shale, pore structure, controlling factors, Qinshui Basin

HIGHLIGHTS

(1) Introduce standard deviation to characterize the coefficient of shale heterogeneity.
(2) TOC and minerals affect the pore structure mainly through their effect on micropores.
(3) Illite-smectite in clay minerals is the main controller of characterization of the pore.

1 INTRODUCTION

The increased energy and environmental demands promoted rapid development of the shale gas industry (Sun et al., 2017; Liu J. et al., 2019; Zhang J. et al., 2019; Xie et al., 2021). Unlike conventional reservoirs, shale gas is mainly stored in adsorbed and free states in complex pore systems (Ding et al., 2013; Wang et al., 2015; Chen et al., 2016; Sun et al., 2021; Tang et al., 2021). The shale has a complex pore structure system dominated by nanoscale pores, varying lithofacies, total organic carbon (TOC) content, and mineral composition, which together result in heterogenous pore morphology, pore size distribution (PSD), pore volume (PV), and specific surface area (SSA), which directly affect the subsequent exploration and development of shale gas (Nelson, 2009; Dang et al., 2016; Hu et al., 2017; Zhang M. et al., 2019; Qin et al., 2020). The characterization of the pore structure plays an important role in shale gas reservoir evaluation and is one of the main factors controlling the enrichment of shale gas (Zhang et al., 2018; Guan et al., 2020; Li et al., 2020; Phaye et al., 2021). Due to the heterogeneity of the pore structure of shales, it is problematic to interpret the occurrence mechanism of shale gas (Liu et al., 2018; Liu R. et al., 2019; Tang et al., 2019; Ge et al., 2020; Luo et al., 2021). Therefore, it is necessary to carry out characterization of shale heterogeneity, and the degree of this strong heterogeneity needs to be investigated in detail.

The heterogeneity of shales has been studied on different scales. The macroscale heterogeneity of shales is mainly manifested in the regional variation of lithology, the total organic carbon (TOC) content, and the organic matter type (Xi et al., 2017a; Luo et al., 2017; Zhang et al., 2018; Yan et al., 2021). The microscale heterogeneities of shales mainly include mineral composition, lithology, organic matter content, and the physical properties of pore structures. Quantitative and qualitative methods for determining pore properties in shales, such as the specific surface area (SSA) or pore volume (PV), can be subdivided into three types, namely, image analysis, intrusive methods, and nonintrusive methods (Liu et al., 2015; Tang S. et al., 2016; Yang R. et al., 2017; Wang et al., 2017; Ju et al., 2018; Zhang and Fu, 2018). Among these methods, the electron microscopy methods (e.g., scanning electron microscopy (SEM), field emission scanning electron microscopy (FE-SEM), and computerized tomography (CT)) provide qualitative characterization of the pore shape, diameter, distribution, and pore connectivity of shales (Curtis et al., 2012; Milliken et al., 2013; Jiang et al., 2017; Wang et al., 2018). Pore properties can be quantified by indirect methods, including small-angle neutron scattering/ultra-small-angle neutron scattering (SANS/USANS) and intrusive methods (especially mercury intrusion and N_2 and CO_2 gas adsorption methods) (Tang X. et al., 2016; Jiang et al., 2017; Yang R. et al., 2017; Zhang L. et al., 2017; Sun et al., 2018). Each method provides information typically for a specific pore diameter range, and hence, in recent years, multiple techniques have been used to analyze the properties of shale pores over the complete pore diameter range (Yang et al., 2017b; Liu et al., 2021a; Liu et al., 2021b).

In recent years, many studies have attempted to characterize shales using these methods, thus recognizing the significance of pore structure characterization for the evaluation of shale gas reservoirs. Loucks et al. (2009) studied the origin and characteristics of nanopores in the Mississippian Barnett Shale, and intraparticle organic nanopores and pyrite-framboid intercrystalline pores contribute to gas storage in Barnett mudstones. Guo et al. (2018) indicated the characteristics of the pore of coal-bearing shales in Turpan-Hami Basin, NW China. Tang et al. (2019) revealed the characteristics of marine shale and the shale gas adsorption capacity in the Upper Yangtze region, China. Ge et al. (2020) studied the characteristics of the transitional shale in southern North China, reporting that shale reservoirs have strong heterogeneity, and analyzed its main controlling factors, which are organic matter maturity and mineral composition.

Individual qualitative and quantitative methods have shown that shales are highly heterogenous at the microscopic scale (Liu et al., 2020; Dang et al., 2021). However, these methods can only reflect marine shales and the middle-to-high maturity stage of the coal-bearing shale heterogeneity to a limited extent. Knowledge of the variability of pore properties of overmature coal-bearing shales is relatively low, and there has been a lack of systematic research integrating the results from various methods to give a more complete picture of the heterogeneity of overmature coal-bearing shales. In addition, the degree of pore heterogeneity in shale gas reservoirs remains unclear in relation to the intrinsic linkage of various influencing factors. It can be seen that addressing these issues is very helpful for predicting the prospect area and reducing the risk in overmature coal-bearing shale gas exploration.

In this study, XRD, FE-SEM, MIP, and N_2-/CO_2-GA introduce standard deviation that has been used to determine the full-sized pore structure of the overmature coal-bearing shale using samples from the Taiyuan and Shanxi Formations from the Wuxiang block, south-central Qinshui Basin, China. In addition, the key factors that control the pore structure of the shale in Wuxiang block, south-central Qinshui Basin, China, have been identified.

2 GEOLOGICAL SETTING

The Wuxiang Block is located on the east flank of the central section of the Qinshui composite slope, south-central Qinshui Basin (**Figure 1**). Faults are relatively well-developed in the study area. The orientations of the faults are primarily NE and NNE trends. The coal-bearing source rocks were mainly deposited in

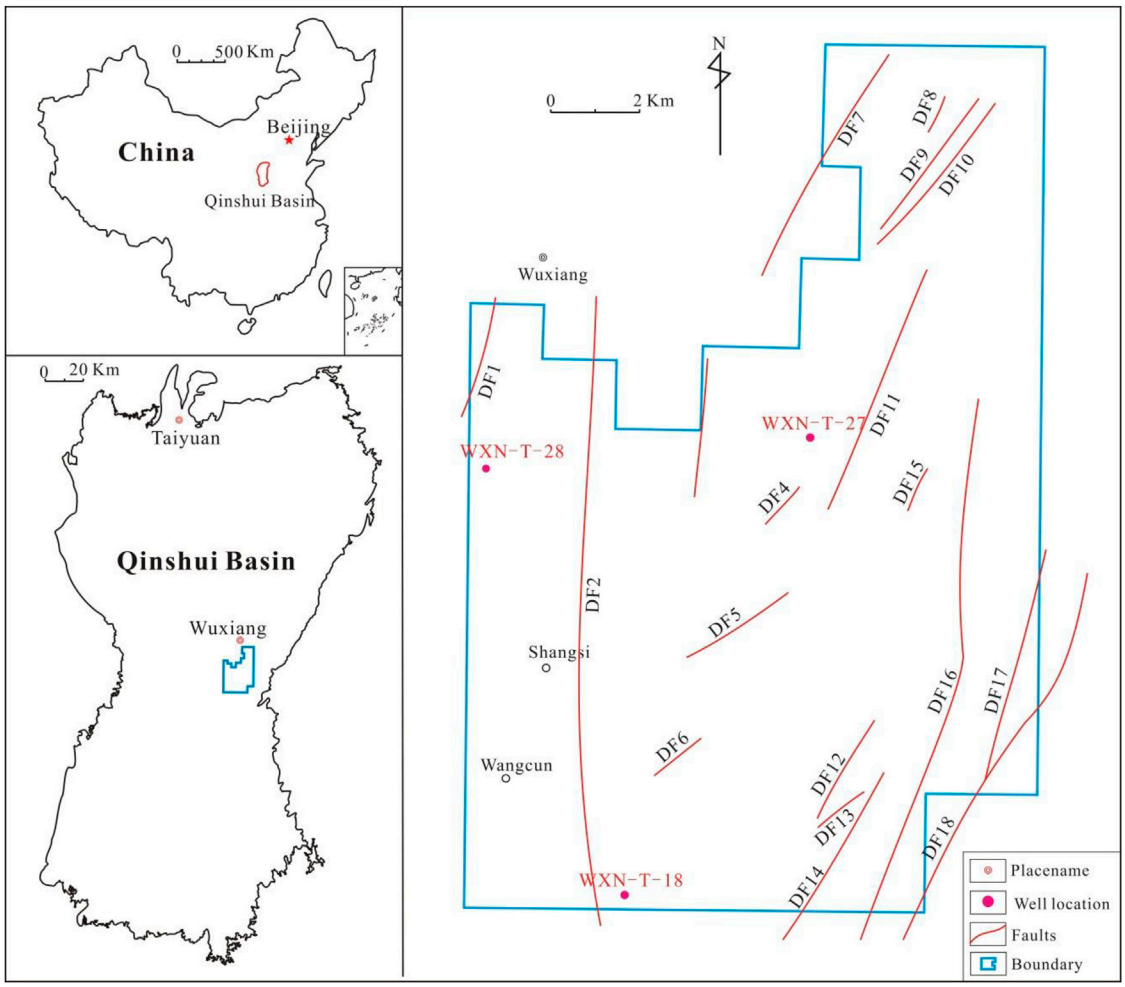

FIGURE 1 | Geological structure of the Wuxiang block in Qinshui Basin, China.

Taiyuan and Shanxi Formations. The Taiyuan Formation was primarily developed by the barrier coast and carbonate platform system which consists of shale, sandstone, limestone, and coal seams. The Shanxi Formation is dominated by river-delta marsh sediments, which contain sandstone and coal, and three to five sets of shale with a thickness of 30–40 m. The thickness of the argillaceous layer in the Shanxi and Taiyuan Formations is 12–82 m (average 36 m) and 46–122 m (mean 79 m), respectively.

3 SAMPLES AND METHODS

3.1 Samples

A total of 11 fresh shale core samples were collected from two wells at a burial depth of 1,580–1,910 m in the Wuxiang block of the south-central Qinshui Basin, China. The well locations are shown in **Figure 1**. A series of experiments including TOC, Ro, XRD, N_2-/CO_2-GA, MIP, and FE-SEM were carried out.

3.2 Experimental Methods

A LECO CS230 carbon/sulfur analyzer was used to measure the TOC content of the samples based on the method GB/T 19145-2003 of China National Standards. Vitrinite reflectance was determined using an MPV-SP microphotometer following ASTM D2799-13 (2013). The Bruker AXS D8 Discover X-ray diffractometer was used to determine mineralogies. Mineral and relative mineral percentages were estimated for each sample according to SY/T 5163-2018. Zeiss Merlin FE-SEM was used to analyze the pore types and morphology at the nanoscale. The experimental conditions of FE-SEM were 24°C and 35% humidity. All observations and analyses were in accordance with SY/T 5162-1997.

A Micromeritics AutoPore IV 9500 V2.03.01 porosity instrument was used to perform the MIP experiment. The PSD of pores ranging from 6 nm to 201 μm was measured. The experiment was conducted in accordance with the standard CB/T 21650.1-2008/ISO 15901-1: 2005. The temperature was 35°C, and the pressure range was 0.90 ~ 30000 psia. N_2 adsorption/desorption experiments were carried out using a Micromeritics ASAP 2460 V2.02 system, and a Micromeritics ASAP 2020 V4.03 system was used for low-pressure CO_2 adsorption/

TABLE 1 | Vitrinite reflectance, TOC, and Rock-Eval pyrolysis data for the shale samples.

Sample	Depth(m)	*Ro*	TOC(%)	T_{max} (°C)	S_1 (mg/g)	S_2 (mg/g)	HI(mg/g)
WXN-18-03	1581.6	2.35	6.61	549	0.01	1.53	23
WXN-18-06	1600.3	2.41	0.29	562	0.01	0.11	38
WXN-18-08	1614.4	2.48	7.42	550	0.01	1.25	17
WXN-18-11	1652.7	2.33	1.74	564	0.01	0.27	15
WXN-18-17	1656.7	2.34	7.54	569	0.04	1.75	23
WXN-18-22	1738.2	2.42	0.73	557	0.01	0.14	19
WXN-28-02	1748.5	2.39	2.01	557	0.03	0.5	25
WXN-28-07	1752.8	2.33	8.36	565	0.03	1.56	19
WXN-28-13	1884.4	2.59	1.57	580	0.03	1.56	19
WXN-28-15	1888	2.54	2.82	585	0.02	0.49	17
WXN-28-19	1900.6	2.63	6.30	580	0.04	0.97	15

Note: TOC, total organic carbon; Ro, vitrinite reflectance; T_{max}, the temperature at the peak of S_2; S_1, free hydrocarbons; S_2, hydrocarbons from pyrolysis; HI, hydrogen index.

desorption experiments. Prior to the experiments, all shale samples were dried and degassed for 72 h. The N_2 and CO_2 adsorption/desorption isotherms were measured at 77 and 273 K, respectively. The relative pressure (P/P_o) of N_2 adsorption/desorption isotherms ranges from 0.011 to 0.995 and that of CO_2 adsorption/desorption isotherms ranges from 0.0001 to 0.032. Brunauer–Emmett–Teller (BET) and Barrett–Joyner–Halenda (BJH) algorithms were used to calculate the SSA and PSD from N_2 adsorption, respectively. (Liu J. et al., 2019). The Dubinin–Astakhov (D-A) model and the density functional theory (DFT) method were used for CO_2 adsorption data (Zhang M. et al., 2019; Song et al., 2019).

The standard deviation is the arithmetic square root of the arithmetic mean of the square of the deviation from the mean. It is represented by σ. The standard deviation is the most commonly used form of quantification that reflects the degree of dispersion of a set of data and is an important indicator of accuracy. We introduce the standard deviation combined with pore volume data for our samples to characterize the shale pore heterogeneity (**Eq. 1**).

$$\sigma_{pv} = \sqrt{\frac{\sum_{i=1}^{n}(x_i - \bar{x})^2}{\mathrm{n}}}, \quad (1)$$

where $\bar{x}$ is the mean of the pore volume, and x_i is pore volume data for the i^{th} sample.

4 RESULTS

4.1 Geochemical Characteristics and Mineral Compositions

The TOC of the 11 samples ranges from 0.29 to 8.36%, with an average of 3.84% (**Table 1**). All of the samples are overmature for oil and gas generation, with *R*o values ranging from 2.33 to 2.65% (average 2.44%), thus indicating that the transitional shales of the Wuxiang block have experienced strong thermal degradation. As a result, the pore structure has been affected by diagenesis and thermal maturation over a wide range of pressures and temperatures. The T_{max} of the shale samples vary from 549 to 580°C, illustrating that the organic matter were in the post-maturity stage with a high degree of hydrocarbon conversion, and a large amount of gas has been generated from the organic matter. As can be seen from **Figure 2**, the kerogen type of the OM is type III kerogen.

Table 2 lists the mineral compositions. Clay and quartz are the main minerals (**Figure 3**). The clay mineral content ranges from 43 to 85.5% with an average of 52.1%, and the quartz content ranged from 12.6 to 61.2%, with the mean value of 43.5%. There is a low abundance of feldspar (0–2.4%), siderite (0–11.3%), and pyrite (0–5.3%). The clay compositions mainly consist of illite-smectite (I/S) and illite, with percentages ranging from 22.5 to 55.6% (mean value of 41.4%), and 8.7–52.7% (mean value of 32%), respectively, followed by kaolinite (8.5–29.8%; mean value 17.7%) and some chlorite (2.6–11.8%; mean value of 8.1%).

4.2 Pore Morphology

A large number of intraparticle pores (IntraP pores) and interparticle pores (InterP pores) were observed in clay minerals of all shale samples. They include interbedded pores (**Figure 4E**), interparticle pores between clay mineral fragments (**Figure 4F**), and dissolution-related IntraP pores (**Figure 4A**). Abundant pores with wedge or slit shapes were observed in either illite or I/S (**Figure 4I**). The wedge-shaped pore size is 50 nm–5 μm, and the slit length can be up to 15 μm. In addition, intergranular pores in strawberry pyrite were observed in the shale (**Figure 4C**). However, pores in the organic matter were only observed in samples WXN-18-03, WXN-18-08, and WXN-28-19 with a high TOC content (**Figures 4B,H**). In general, the development of OM pores is related to the TOC content and thermal maturity. When *R*o is greater than 2%, the number of OM pores will decrease as the *R*o increases (Jarvie et al., 2007; Ge et al., 2020). Moreover, a number of microcracks were observed (**Figures 4B,D**). These microcracks can be divided into two types: shrinkage cracks and cracks between organic matter and clay. The shrinkage cracks were probably formed by the dewatering of clay minerals. InterP pores and microcracks have better interconnection for the pore network than that of IntraP pores.

4.3 Pore Structure Characteristics

4.3.1 Macropore Structure Based on MIP Measurements

Based on the plots of cumulative mercury volume intruded versus pore diameter (**Figure 5**), pore structures of all the samples were divided into two types.

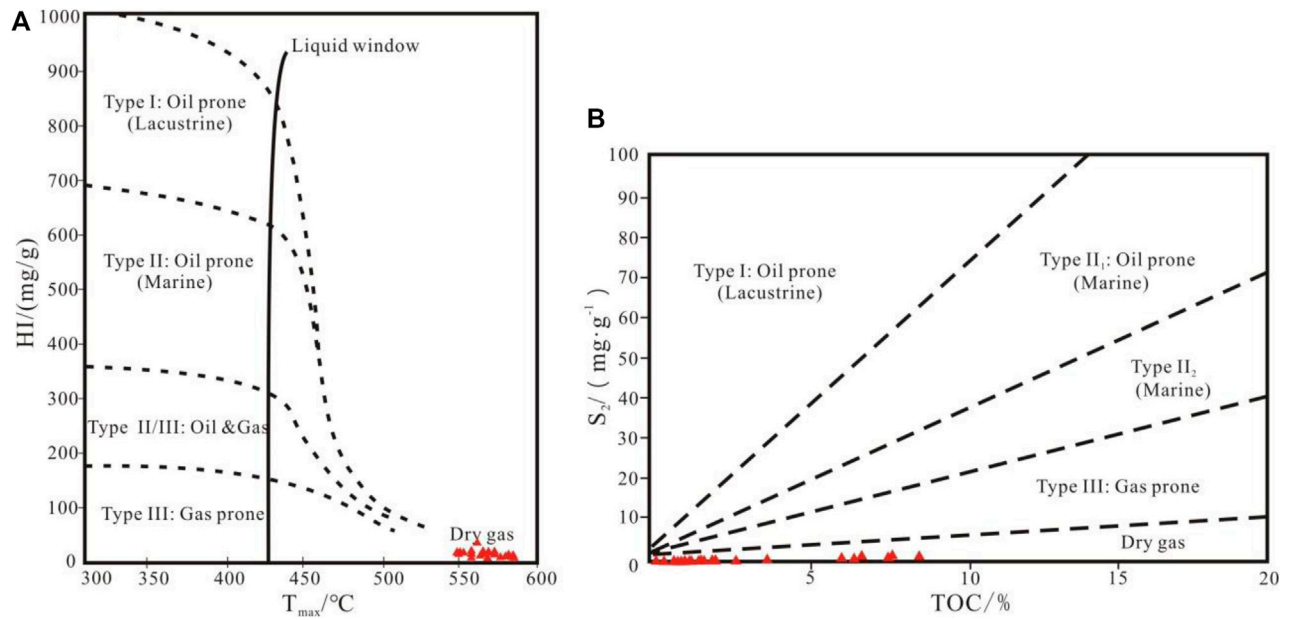

FIGURE 2 | Plot of T_{max}°C and HI and plot of TOC and S_2 [modified from Mendhe et al. (2017)]. Rock-Eval plots for the samples: **(A)** HI versus T_{max}, and **(B)** S_2 versus TOC content.

TABLE 2 | Mineralogical composition of shales in the Wuxiang block.

Sample	Mineral composition (wt%)						Clay composition (wt%)			
	Qtz	Fs	Cbg	Other	Py	Clay	I	I/S	K	C
WXN-18-03	34.6	1.1	0.3	0.6	1	62.4	28.4	55.1	13.9	2.6
WXN-18-06	53.3	1.4	0.3	0.3	—	44.7	51.7	37.1	8.5	2.7
WXN-18-08	49	0.3	0.9	—	5.3	44.5	34.2	38.8	17.3	9.7
WXN-18-11	39.4	1.1	0.9	0.9	2.3	55.4	19.4	52.2	13.3	5.1
WXN-18-17	12.6	—	0.6	—	1.3	85.5	8.7	55.6	25.1	10.6
WXN-18-22	61.2	1.8	0.6	0.4	0.9	35.1	52.7	22.5	20	4.8
WXN-28-02	44.5	1.9	0.6	0.5	—	52.5	43.2	33.7	12.2	10.9
WXN-28-07	38.2	2.4	5.7	10.7	—	43	38.4	23	22.3	16.3
WXN-28-13	51.2	.4	0.4	1.2	1.7	45.1	31.5	37.3	22.8	8.4
WXN-28-15	48.9	—	—	3.1	—	48	26.5	31.9	29.8	11.8
WXN-28-19	55.7	—	0.4	—	—	43.9	30.8	42.8	16.2	10.2

Note: Qtz, quartz; Fs, feldspar; Cbg, carbonate group; Py, pyrite; I, illite; I/S, illite/smectite; K, kaolinite; C, chlorite;/: not detected.

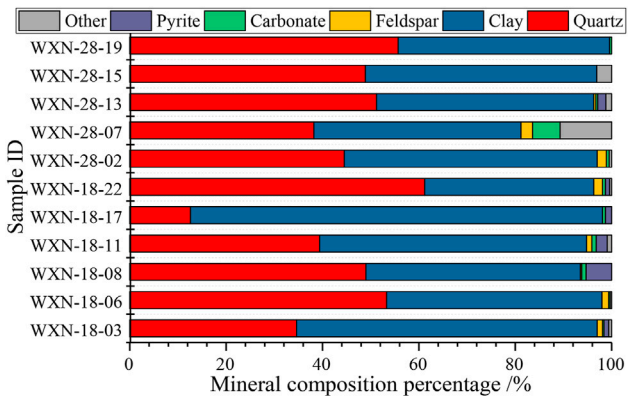

FIGURE 3 | Mineral composition percentage of the shale samples.

For the first type of curve, the volume of mercury intruded increases as the pore diameter decreases (**Figure 5A**). These characteristics reflect the good connectivity between the pores; the ends of the pores are mostly open, and these samples contain a mixture of slit-shaped and ink bottle-shaped pores. As can be seen from **Figure 5B**, the second-type of curve has narrow hysteresis loops. Due to the relatively well-developed microfractures in this type of shale (**Figure 4D**), mercury mainly intrudes into pores larger than 10 μm. The microfractures may have been formed during the diagenesis process or during the sample preparation process (Xi et al., 2017b). There is almost no mercury injected into the pores ranging from 50 nm to 10 μm in diameter.

Figure 6 shows the PSD of the samples which are obtained from the mercury injection data using dV/d (logD) plots, and two types of curves are observed. The first type (**Figure 6A**) shows the presence of a small amount of mercury in the macropores; however, it is mainly

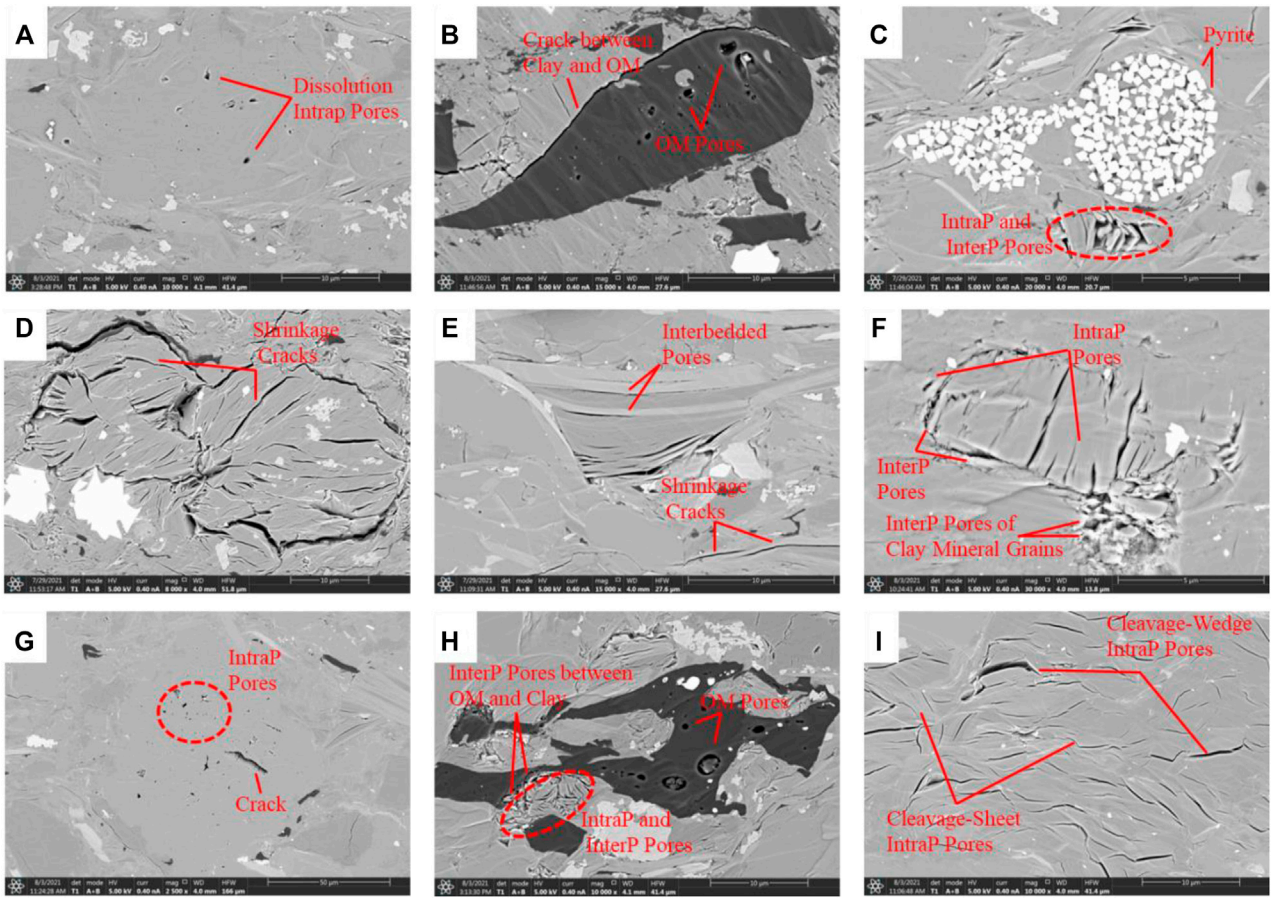

FIGURE 4 | FE-SEM images of the coal-bearing shales from the Wuxiang block. FE-SEM images of the coal-bearing shales from the Wuxiang block: **(A)**, WXN-18-06; **(B–D)**, WXN-18-08; **(E)**, WXN-18-22; **(F)**, WXN-28-13; **(G)**, WXN-28-15; **(H,I)**, WXN-28-19.

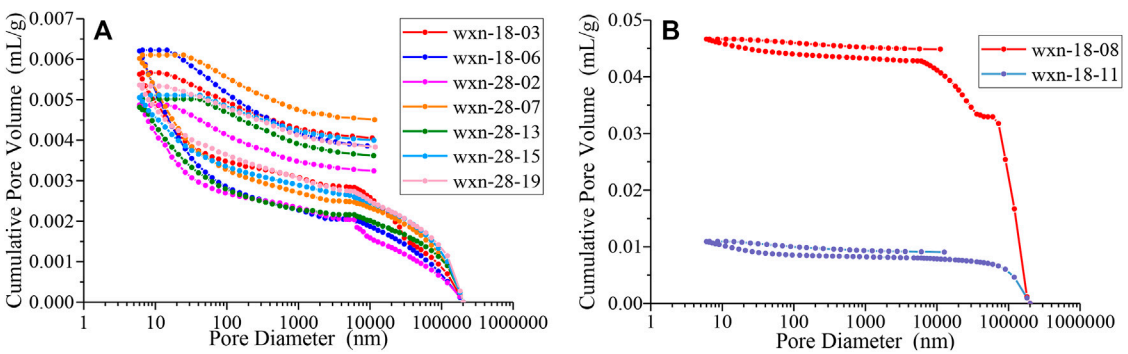

FIGURE 5 | Two different relationships between mercury intrusion and extrusion and the pore diameters based on MIP. Two different relationships between mercury intrusion and extrusion and the pore diameters based on MIP **(A)** wide hysteresis loops, **(B)** narrow hysteresis loops.

intruded into the mesopores. As can be seen from **Figure 6B**, the macropore volume of the second type shale is mainly controlled by pores with a pore size greater than 10 μm, while pores between 50 nm and 10 μm are not developed. Although they both have a peak near 10 μm, the pores of WXN-18-08 are more developed in the 50–100 nm range than WXN-18-11.

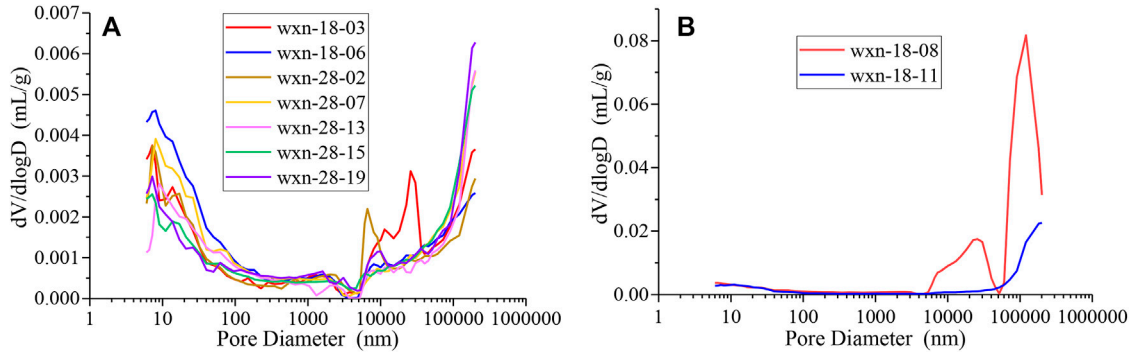

FIGURE 6 | PSD of the samples based on MIP. PSD of the samples based on MIP **(A)** wide hysteresis loops, **(B)** narrow hysteresis loops.

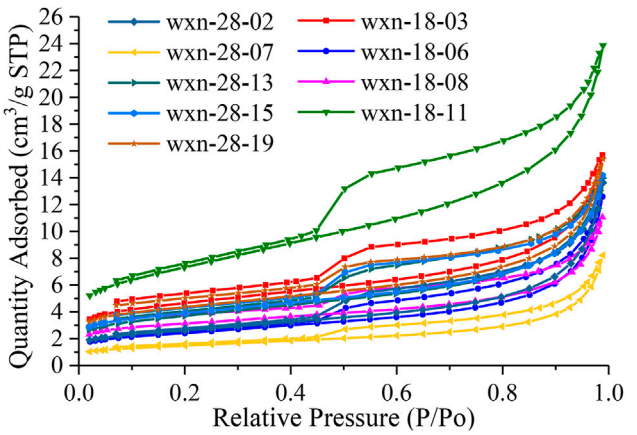

FIGURE 7 | N_2 adsorption–desorption isotherms of nine representative shale samples.

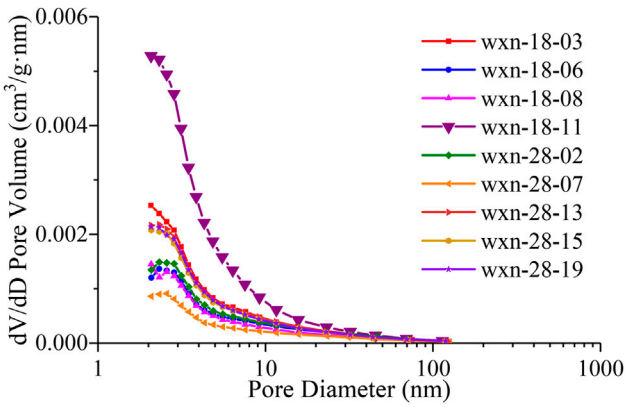

FIGURE 8 | PSD obtained from low-pressure N_2 adsorption isotherms of the coal-bearing shale samples.

4.3.2 Mesopore Structure Based on N_2 Adsorption Isotherms

Figure 7 shows the N_2 adsorption and desorption isotherms, which are generally "S"-shaped. Based on the IUPAC classification, the N_2 adsorption isotherms of the samples belong to type IV isotherms, which indicates that the shale pores are distributed continuously and are classified as mesopores (Rouquerol et al., 1994). The hysteresis loop has been used to characterize pore shapes (Liu J. et al., 2019). Based on the classification of hysteresis loops by IUPAC, the nine samples can be divided into the H2 type or H3 type, which are dominated by slit-shaped pores, wedge-shaped pores, and narrow neck pores.

The PSD of the samples can be obtained by analyzing the N_2 adsorption and desorption curves using the BJH model. However, studies have shown that the PSD curves, calculated by desorption isotherms that are affected by tensile strength, cannot accurately reflect the real pore size distribution in porous media (Groen et al., 2003; Wang et al., 2015; Xi et al., 2017b). The PSD calculated from N_2 adsorption for each of the nine samples is illustrated in

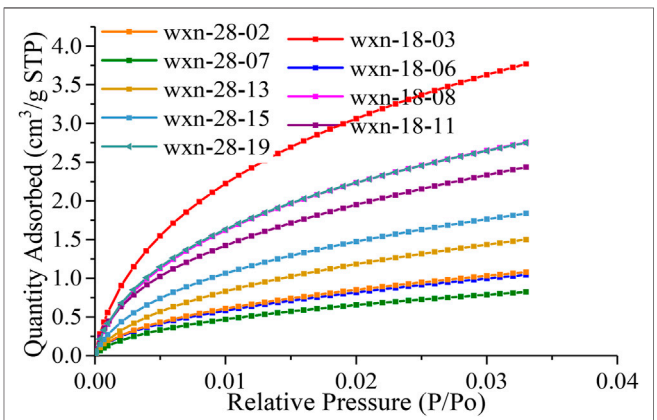

FIGURE 9 | CO_2 adsorption–desorption isotherms of the coal-bearing shale samples.

Figure 8. The PSD distribution curves of all samples showed a single-peak curve with the main peak at 2 ~ 3 nm.

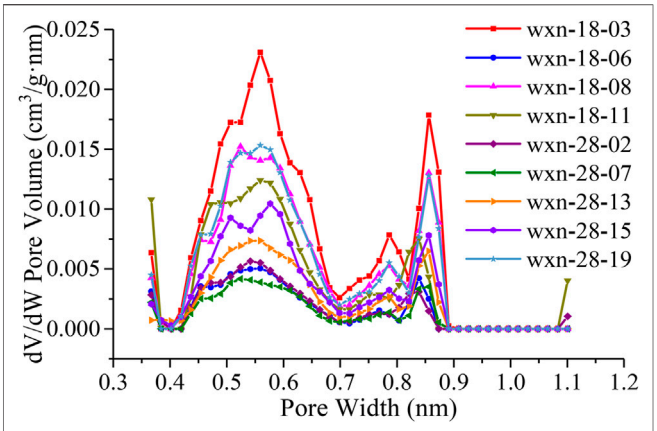

FIGURE 10 | PSD derived from CO_2 adsorption using the DFT model.

4.3.3 Micropore Structure Based on CO_2 Adsorption Isotherms

Figure 9 shows that the CO_2 adsorption isotherms of nine shale samples belong to type I, which indicates the existence of open micropores with monolayer adsorption. **Figure 10** shows the relationship between the dV/dW pore volume and pore width. All samples have three peaks in the pore width range of 0.45–0.60 nm, 0.75–0.80 nm, and 0.82–0.87 nm, respectively. Pore widths less than 0.9 nm are the main contributors to micropore volume. When the pore size is larger than 0.9 nm, the volume of micropores does not change with the increase in the pore size.

5 DISCUSSION

5.1 Characterization of the Full-Sized Pore Structure

The pore structure of shales has strong heterogeneity, such as the PSD in the shale ranges from nanometer to micrometer scales; macropores, mesopores, and micropores have different contributions to the PV and SSA, respectively (Zhang J. et al., 2017; Zhang J. et al., 2019). The pore is the main place to adsorb and gather gas. Studying pore anisotropy is helpful to understand the accumulation mechanisms of shale gas. Consequently, the PV, SSA, and the standard deviation of the pore volume data (σ_{PV}) of the samples were calculated (**Table 3**), and the coefficient of pore heterogeneity is listed in **Table 4**.

As can be seen from **Figure 11**, the PSD curves contain multiple-peak distribution, with the peaks mainly distributed in the range of 0.4 ~ 0.9 nm, 2 ~ 3 nm, and 5 ~ 30 μm. **Figure 12** shows the PV percentages and SSA percentages for shale samples. Mesopores are the largest contributors to the PV of most samples, except sample WXN-18-08 (**Figure 12A**), which contains microfractures (**Section 4.3.1**), and hence, more macropores larger than 10 μm are present. The mesopore PV ranges from 0.0086 cm^3/g to 0.029 cm^3/g (**Table 3**), accounting for 18.9–77.8% of the total PV, but its contribution to the SSA is less than from micropores (**Figure 12B**). The contribution of micropores to the PV is small, accounting for 6.2–19.5% (**Figure 11A**), but their SSA accounts for 51.8–80.1% (**Figure 12B**). The macropores' PV ranges from 0.0029 cm^3/g to 0.0443 cm^3/g (**Table 3**), and the contribution to the pore volume is secondary only to that of mesopores, but its contribution to the SSA is less than 0.5% (**Figure 12B**).

TABLE 3 | PV and SSA for samples from MIP (macropore), N2 (mesopore) and CO2 (micropore) adsorption experiments.

Sample	Pore volume (cm^3/g)				Specific surface area (m^2/g)			
	Total PV	Macropore (>50 nm)	Mesopore (2-50 nm)	Micropore (<2 nm)	Total SSA	Macropore (>50 nm)	Mesopore (2-50 nm)	Micropore (<2 nm)
WXN-18-03	0.0237	0.0011	0.0175	0.0051	43.5225	0.018	10.002	33.5025
WXN-18-06	0.0161	0.0013	0.0135	0.0012	15.8295	0.032	6.53	9.2675
WXN-18-08	0.018	0.0031	0.0112	0.0037	30.0709	0.038	5.962	24.0709
WXN-18-11	0.033	0.0009	0.029	0.0031	41.8851	0.02	20.156	21.7091
WXN-28-02	0.0173	0.0013	0.0147	0.0013	16.8145	0.018	7.185	9.6115
WXN-28-07	0.011	0.0013	0.0086	0.001	11.776	0.03	4.176	7.57
WXN-28-13	0.0192	0.0011	0.0163	0.0018	22.1414	0.027	9.287	12.8274
WXN-28-15	0.0188	0.0011	0.0153	0.0024	24.268	0.022	8.829	15.417
WXN-28-19	0.021	0.0014	0.0158	0.0037	32.632	0.024	9.077	23.522

TABLE 4 | Coefficient of pore heterogeneity for shale samples.

Sample	σ_{PV}		
	Macropore (>50 nm)	Mesopore (2-50 nm)	Micropore (<2 nm)
WXN-18-03	0.001060546	0.000832395	0.007092993
WXN-18-06	0.001280702	0.000453267	0.001779959
WXN-18-08	0.015711572	0.000465236	0.005118915
WXN-18-11	0.00449908	0.001871608	0.004381028
WXN-28-02	0.00092288	0.000504757	0.001804721
WXN-28-07	0.001245008	0.00030148	0.001467882
WXN-28-13	0.001054573	0.000748229	0.002555286
WXN-28-15	0.00102724	0.000716084	0.003325848
WXN-28-19	0.001163948	.000737036	0.005205515

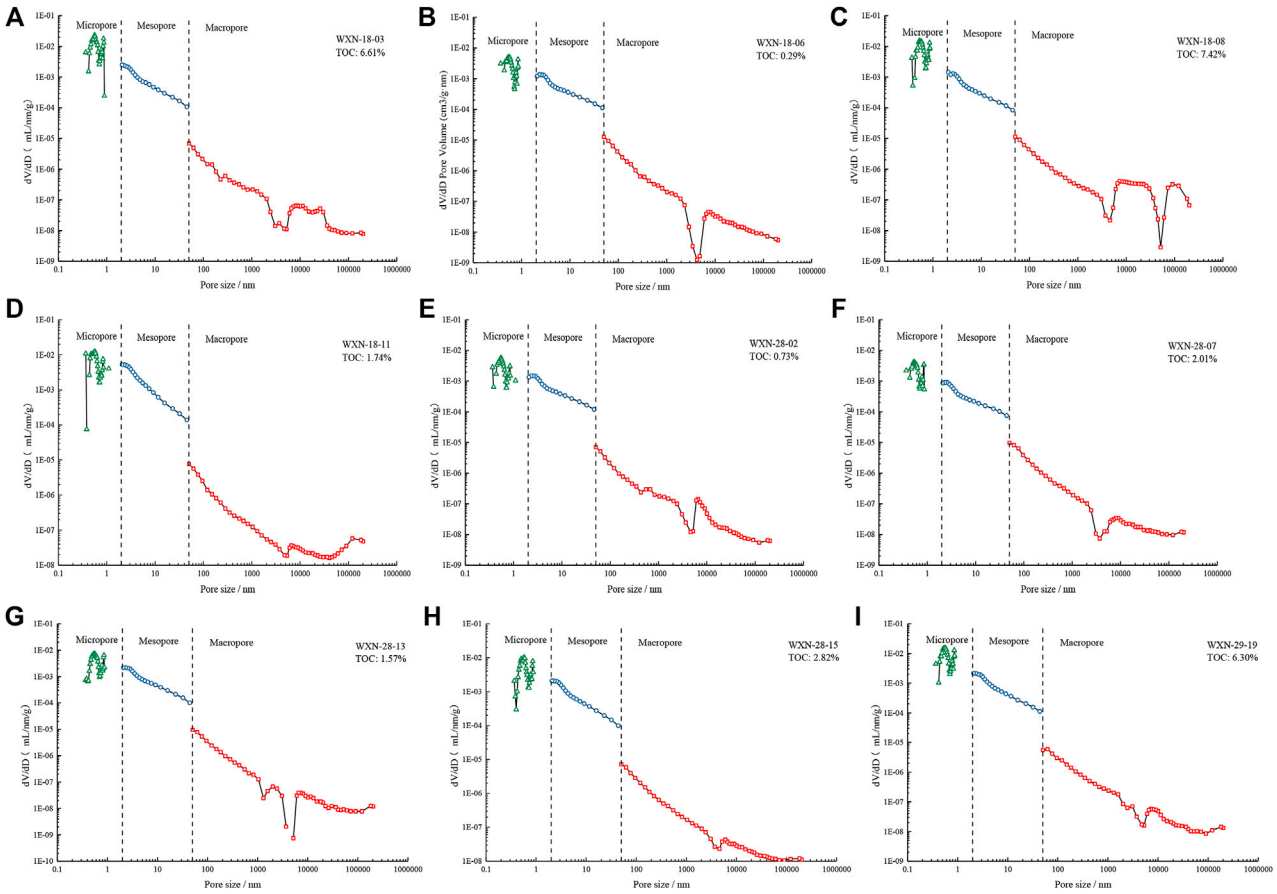

FIGURE 11 | PSD of full-sized pores combining MIP and N_2/CO_2-GA.

5.2 Controlling Factors of the Shale Pore Structure

5.2.1 Effects of the TOC Content on the Pore Structure

It has been reported that the TOC content has an important effect on the pore structure of shales (He et al., 2016; Ge et al., 2020). The effect of the TOC on the SSA and PV is shown in **Figure 13**. A positive relationship exists between the micropore PV, micropore SSA, and TOC content. However, there is no clear correlation for the macropore or mesopore PV or SSA and the TOC content. This is different from previous studies where the TOC in coal-bearing shales with *R*o <2% showed a significant positive correlation with both mesopores and micropores (Zhang M. et al., 2019; Yu et al., 2020). This is because when the maturity is in the immature to petroleum generation maturity stages, a large number of mesopores and micropores are developed in the

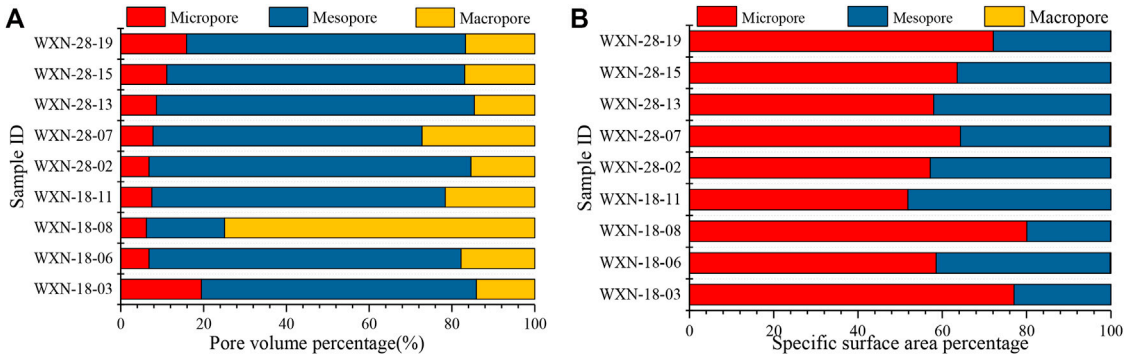

FIGURE 12 | (A) PV percentages and **(B)** SSA percentages for the shale samples in the Wuxiang block.

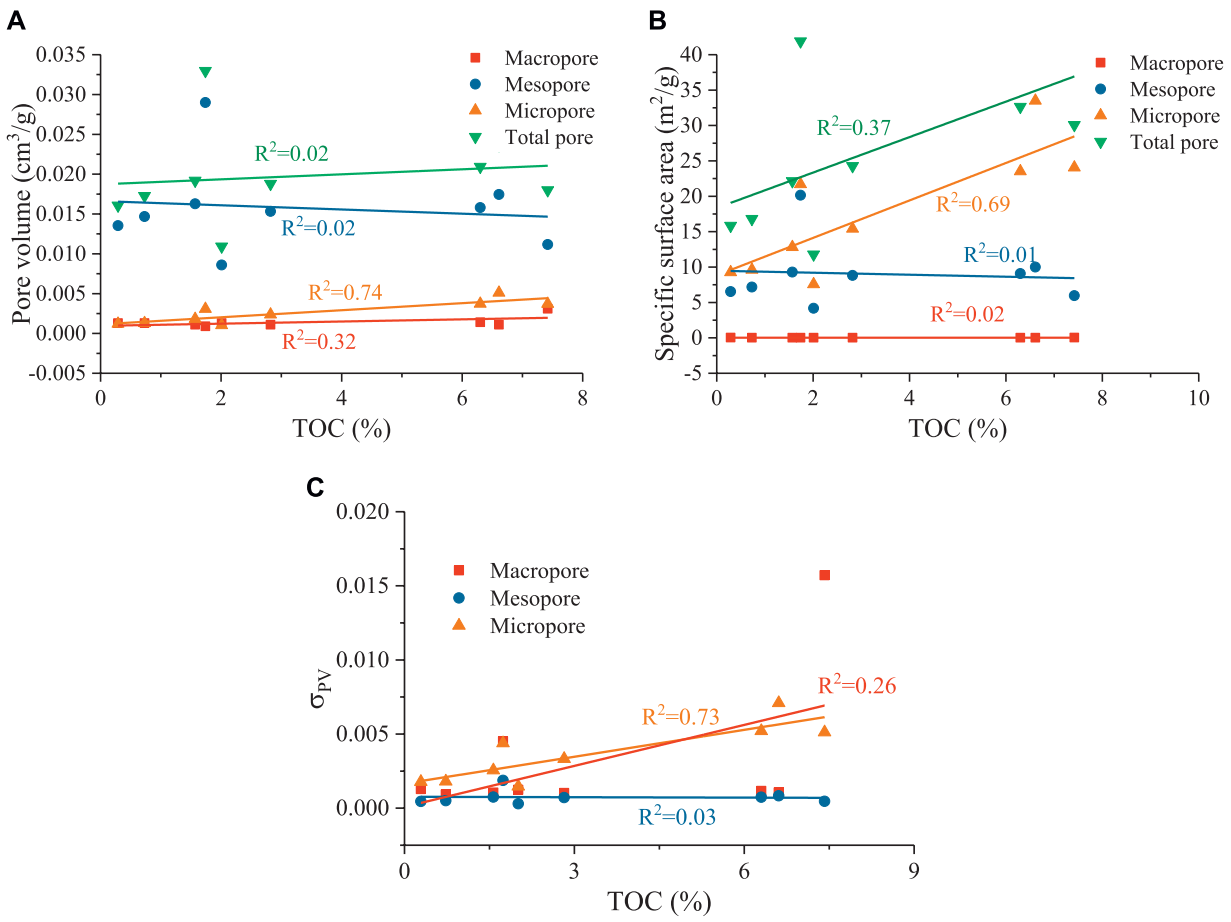

FIGURE 13 | Relationships between the TOC content, **(A)** pore volume, and **(B)** pore specific surface area for the shale samples. **(C)** Relationships between the TOC content and σ_{PV} for the shale samples.

organic matter, but when the shale reaches the overmature stage, the mesopores in the organic matter, in particular, are affected by compaction. Two overmature samples (WXN-28-13 and WXN-28-19) with similar maturity and mineral contents but with significantly different TOC contents (1.57 versus 6.30%, respectively) were selected to investigate the relationship between the TOC content and pore structure in overmature samples. The results show that the total PV, macropore PV, and mesopore PV of the two samples have similar characteristics, but there are obvious differences in the micropore PV. The latter

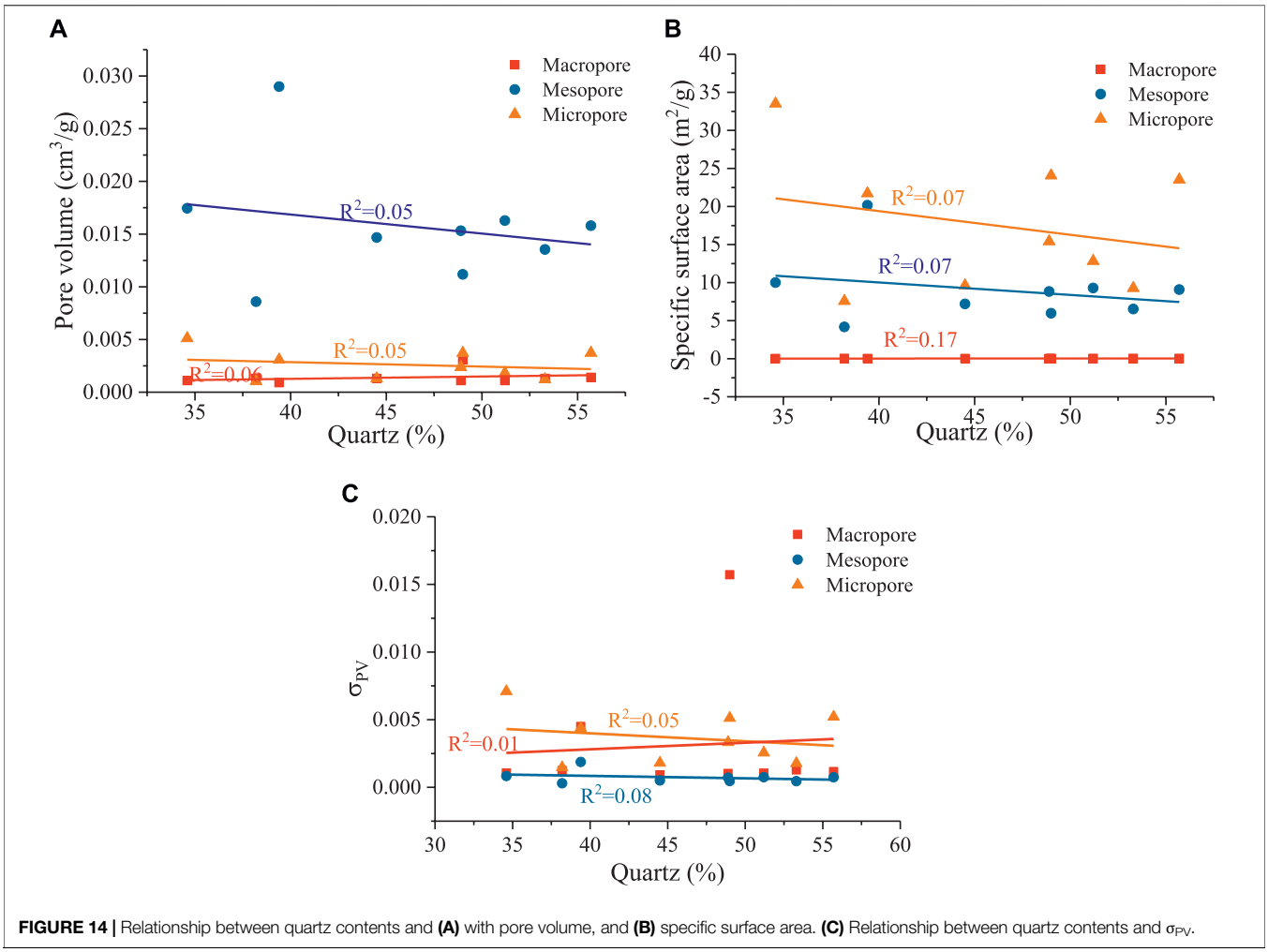

FIGURE 14 | Relationship between quartz contents and **(A)** with pore volume, and **(B)** specific surface area. **(C)** Relationship between quartz contents and σ_{PV}.

value for sample WXN-28-19 (0.00373 cm^3/g) is approximately twice that of sample WXN-28-13 (0.00182 cm^3/g) (**Table 3**). Similarly, the micropore SSA from sample WXN-28-19 is considerably greater than that of sample WXN-28-13. The results show that a higher TOC content results in a higher micropore content for a given mineralogy, which is consistent with the results observed by FE-SEM (organic pores are only observed in samples with a high TOC content). The relationship between the TOC and σ_{PV} (**Figure 13**) shows that the TOC has a significantly positive correlation with the σ_{PV} for micropores, while the correlation with macropores and mesopores is weak, which indicates that the TOC mainly affects the non-homogeneity of micropores. This is consistent with the results of the above study. Earlier work considered that maturity may be the main controlling factor for overmature shale pore development overriding the effects of the TOC content (Xi et al., 2018).

5.2.2 Effects of the Quartz Content on the Pore Structure

The brittle minerals in the shale are dominated by quartz, which can provide support for the reservoir and improve permeability (Yan et al., 2017). **Figure 14** shows that there is no clear relationship between quartz and the PV or SSA. This suggests that the quartz content is not a key parameter that determines the pore structure. **Figure 14** shows that there is no significant relationship between quartz and σ_{PV}, which is consistent with the lack of correlation between PV, SSA, and quartz. Previous studies of samples in the middle-to-high maturity stages show that quartz has a positive relationship with the macropore PV and has a weakly negative correlation or no correlation with the mesopore and micropore PV (Wang et al., 2015; Pan et al., 2017). It is generally believed that this is caused by two reasons: on the one hand, there are few intragranular pores associated with quartz, which are mostly lost by compaction, cementation, or plugging by either inorganic or organic matter such as clay particles or bitumen (Loucks et al., 2009; Wang et al., 2019).

5.2.3 Effects of the Clay Content on the Pore Structure

SEM images show that clay mineral pores are the main pores in these overmature samples (**Figure 4**). The relationship between clay minerals and pore structure properties is shown in **Figure 15**. The SSA of micropores is weakly positively correlated with the

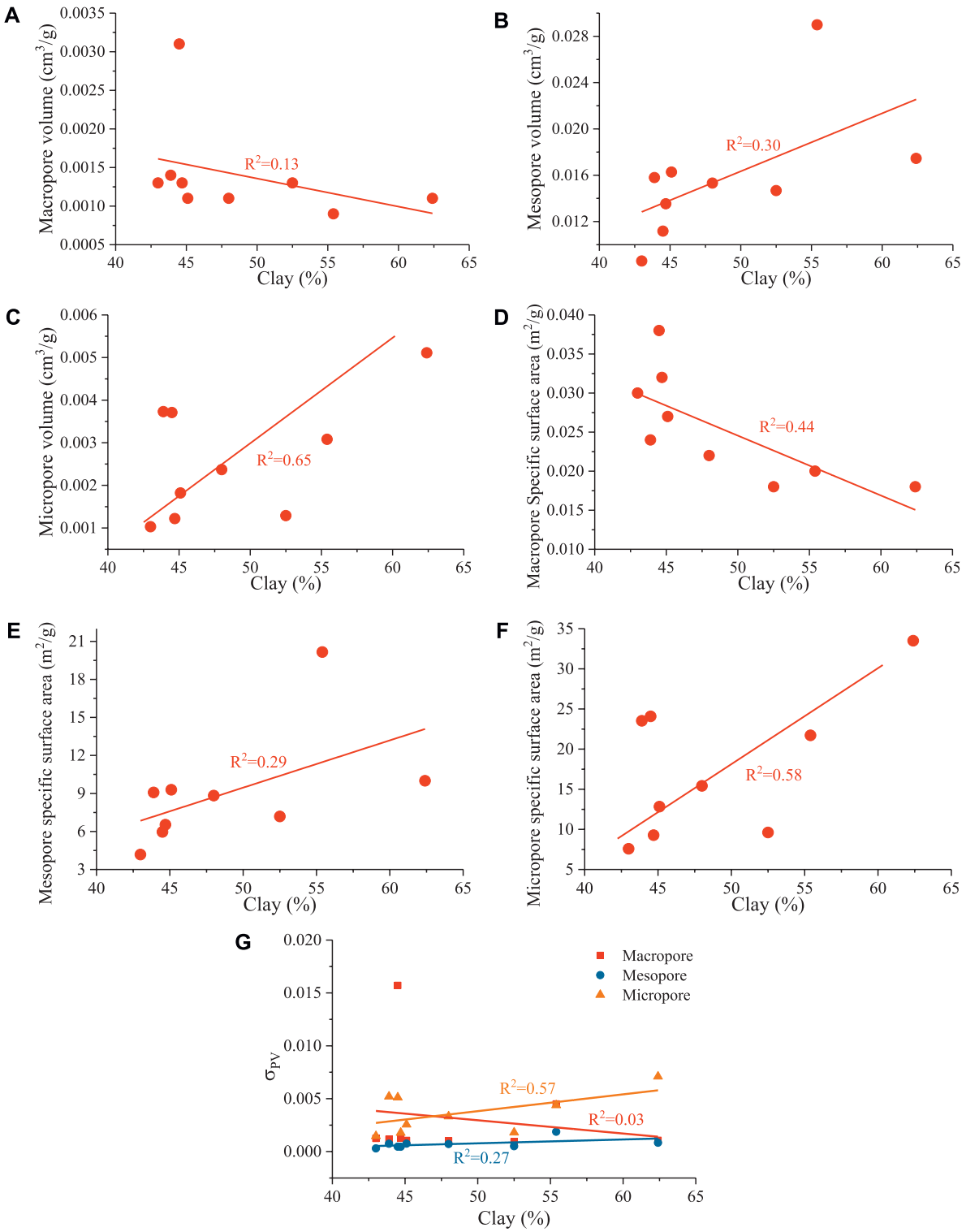

FIGURE 15 | Relationship between clay contents with the pore volume and specific surface area. Relationship between clay contents with the pore volume **(A–C)** and specific surface area **(D–F)** and with σ_{PV} **(G)**.

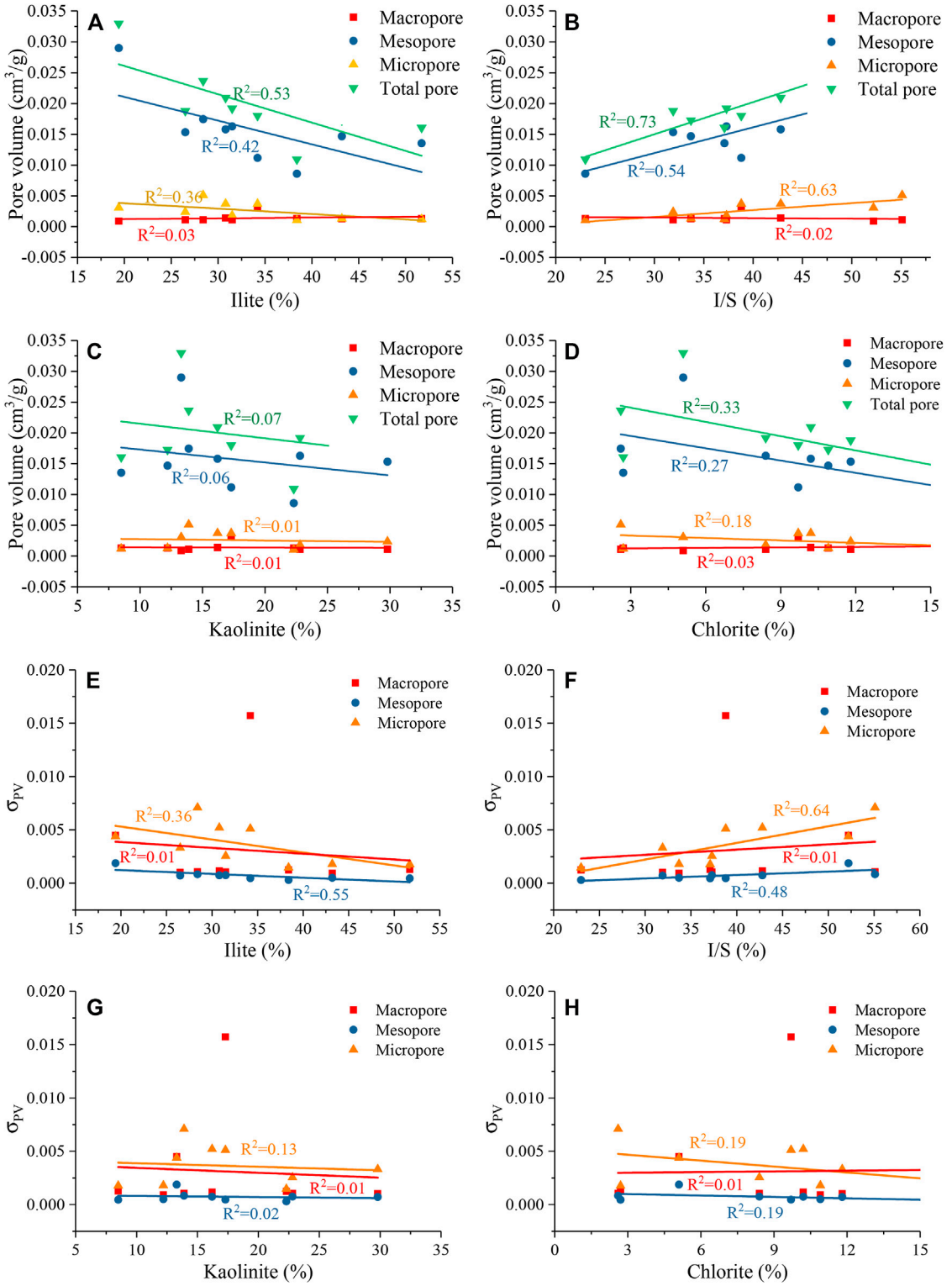

FIGURE 16 | Relationships between clay minerals with pore volume **(A–D)** and σ_{PV} **(E–H)**.

content of clay minerals but not the PV, whereas for other types of pores, there is no obvious correlation with either the PV or SSA. The relationship between clay minerals and coefficient of pore heterogeneity is shown in **Figure 15**, and it can be found that there is a weakly positive correlation between clay minerals and σ_{PV}, which indicates that clay minerals contribute to the pore

heterogeneity mainly through micropores. This differs from the medium-to-high maturity stage of the similar samples, where clay not only affects the development of micropores but also has a significant positive correlation with mesopores. In early diagenesis, clay minerals have various morphologies of micropores, mesopores, and microcracks. When the degree of thermal evolution increases, as the degree of compaction increases, the volume of the macropores gradually decreases, until it disappears (Li et al., 2020). In addition, the combination of clay minerals and soluble organic matter plays an important role in the development of micropores in shales (Ge et al., 2020).

In order to understand which clay minerals play an important role in pore heterogeneity, the correlation between PV, σ_{PV}, and subtypes of clay minerals is shown in **Figure 16**. I/S is positively correlated with the micropore, mesopore, and total PV (**Figure 16B**) However, the content of illite and chlorite has a negative correlation with the micropore, mesopore, and total PV (**Figures 16A,D**). In addition, this study did not find a correlation between kaolinite and pore volume (**Figure 16C**). Also, the plots of clay minerals versus σ_{PV} confirm that I/S is the main clay mineral component affecting pore heterogeneity, especially affecting micropores and mesopores (**Figures 16E–H**). Previous studies have indicated that a large amount of K^+ will be consumed during the process of montmorillonite illitization forming I/S, which will promote the dissolution of feldspar and increase the pore volume (Peltonen et al., 2009; Yang et al., 2017a). Chlorite is mainly produced in late diagenesis. Chlorite itself has a high degree of compaction and a denser arrangement of minerals, resulting in poor pore development (Zhang M. et al., 2019). Therefore, I/S plays a key role in the development of pore properties in overmature samples.

In summary, comprehensive analysis of relationships between the TOC content and mineral composition with pore structure properties (PV, SSA, and σ_{PV}), together with FE-SEM images of the overmature coal-bearing shale, shows that the micropores are mainly developed in clay minerals, and some micropores are also developed in shales with a high TOC content. The I/S content exerts the most significant control on the pore structure. Mesopores are mainly developed in the clay mineral layers, especially in I/S, while increasing the illite content reduces the development of mesopores. Macropores and microfractures are mainly developed in clays and quartz and do not correlate significantly with the TOC and mineral composition due to the influence of compaction and cementation.

6 CONCLUSION

(1) There are great differences in pore morphology between the overmature coal-bearing shale and marine shale. The slit-shaped and wedge-shaped intraP pores in clay minerals are dominant in the shale. OM pores were only developed in some samples with a high TOC content. Shrinkage cracks are commonly formed by dehydration of clay minerals.
(2) Overmature coal-bearing shale reservoirs have very heterogenous pore structures. Mesopores are the largest contributors to the pore volume, but their contribution to the SSA is less than micropores. The contribution of micropores to the PV is low, accounting for 6.2–19.5%, but their SSA accounts for 51.8–80.1%. The macropore contribution to the pore volume is second only to that of the mesopore, but their contribution to the SSA is less than 0.5%.
(3) The pore structure is mainly controlled by i) the differences in mineral composition and ii) diagenesis thermal maturation. The TOC and clay minerals affect the heterogeneity of the pore structure mainly by controlling the abundance of micropores, while quartz has no clear relationship between the pore volume, specific surface area, and σ_{PV}. I/S is the main component in clay minerals that affects the pore properties.

DATA AVAILABILITY STATEMENT

The original contributions presented in the study are included in the article/Supplementary Material, further inquiries can be directed to the corresponding author.

AUTHOR CONTRIBUTIONS

XZ devised the project and wrote a significant part of the study. XL provided the main conceptual ideas and wrote the main part of the manuscript. JY, BZ, JS, and ZY helped with the manuscript, the figures, and data analysis. All authors contributed to the manuscript and approved the submitted version.

FUNDING

This research was financially supported by the National Natural Science Foundation of China (Nos. U1810201 and 41572125), the National Science and Technology Major Project of China (No. 2016ZX05007-003), the Science and Technology Project of PetroChina (No. T11083), and the Fundamental Research Funds for the Central Universities (Nos. 2020YJSMT02 and 2021YJSMT09).

ACKNOWLEDGMENTS

We thank Dr. Jizhen Zhang and Dr. Qiang Wei for their help and suggestions on the original manuscript. All the editors and reviewers are gratefully acknowledged.

REFERENCES

Chen, Q., Zhang, J., Tang, X., Dang, W., Li, Z., Liu, C., et al. (2016). Pore Structure Characterization of the Lower Permian Marine-Continental Transitional Black Shale in the Southern North China Basin, Central China. *Energy Fuels* 30 (12), 10092–10105. doi:10.1021/acs.energyfuels.6b01475

Curtis, M. E., Sondergeld, C. H., Ambrose, R. J., and Rai, C. S. (2012). Microstructural Investigation of Gas Shales in Two and Three Dimensions Using Nanometer-Scale Resolution Imaging. *Bulletin* 96 (4), 665–677. doi:10.1306/08151110188

Dang, W., Jiang, S., Zhang, J., Li, P., Nie, H., Liu, Y., et al. (2021). A Systematic Experimental and Modeling Study of Water Adsorption/desorption Behavior in Organic-Rich Shale with Different Particle Sizes. *Chem. Eng. J.* 426, 130596. doi:10.1016/j.cej.2021.130596

Dang, W., Zhang, J., Tang, X., Chen, Q., Han, S., Li, Z., et al. (2016). Shale Gas Potential of Lower Permian marine-continental Transitional Black Shales in the Southern North China Basin, central China: Characterization of Organic Geochemistry. *J. Nat. Gas Sci. Eng.* 28, 639–650. doi:10.1016/j.jngse.2015.12.035

Ding, W., Zhu, D., Cai, J., Gong, M., and Chen, F. (2013). Analysis of the Developmental Characteristics and Major Regulating Factors of Fractures in marine-continental Transitional Shale-Gas Reservoirs: A Case Study of the Carboniferous-Permian Strata in the southeastern Ordos Basin, central China. *Mar. Pet. Geology.* 45, 121–133. doi:10.1016/j.marpetgeo.2013.04.022

Ge, T., Pan, J., Wang, K., Liu, W., Mou, P., and Wang, X. (2020). Heterogeneity of Pore Structure of Late Paleozoic Transitional Facies Coal-Bearing Shale in the Southern North China and its Main Controlling Factors. *Mar. Pet. Geology.* 122, 104710–104713. doi:10.1016/j.marpetgeo.2020.104710

Groen, J. C., Peffer, L. A. A., and Pérez-Ramı´rez, J. (2003). Pore Size Determination in Modified Micro- and Mesoporous Materials. Pitfalls and Limitations in Gas Adsorption Data Analysis. *Microporous Mesoporous Mat* 60 (1-3), 1–17. doi:10.1016/s1387-1811(03)00339-1

Guan, M., Liu, X., Jin, Z., and Lai, J. (2020). The Heterogeneity of Pore Structure in Lacustrine Shales: Insights from Multifractal Analysis Using N2 Adsorption and Mercury Intrusion. *Mar. Pet. Geology.* 114, 104150–104158. doi:10.1016/j.marpetgeo.2019.104150

Guo, X., Huang, Z., Ding, X., Chen, J., Chen, X., and Wang, R. (2018). Characterization of Continental Coal-Bearing Shale and Shale Gas Potential in Taibei Sag of the Turpan-Hami Basin, NW China. *Energy Fuels* 32 (9), 9055–9069. doi:10.1021/acs.energyfuels.8b01507

He, J., Ding, W., Zhang, J., Li, A., Zhao, W., and Dai, P. (2016). Logging Identification and Characteristic Analysis of marine-continental Transitional Organic-Rich Shale in the Carboniferous-Permian Strata, Bohai Bay Basin. *Mar. Pet. Geology.* 70, 273–293. doi:10.1016/j.marpetgeo.2015.12.006

Hu, H., Hao, F., Lin, J., Lu, Y., Ma, Y., and Li, Q. (2017). Organic Matter-Hosted Pore System in the Wufeng-Longmaxi (O 3 W-S 1 1) Shale, Jiaoshiba Area, Eastern Sichuan Basin, China. *Int. J. Coal Geology.* 173, 40–50. doi:10.1016/j.coal.2017.02.004

Jarvie, D. M., Hill, R. J., Ruble, T. E., and Pollastro, R. M. (2007). Unconventional Shale-Gas Systems: The Mississippian Barnett Shale of north-central Texas as One Model for Thermogenic Shale-Gas Assessment. *Bulletin* 91 (4), 475–499. doi:10.1306/12190606068

Jiang, S., Tang, X., Cai, D., Xue, G., He, Z., Long, S., et al. (2017). Comparison of marine, Transitional, and Lacustrine Shales: A Case Study from the Sichuan Basin in China. *J. Pet. Sci. Eng.* 150, 334–347. doi:10.1016/j.petrol.2016.12.014

Ju, Y., Sun, Y., Tan, J., Bu, H., Han, K., Li, X., et al. (2018). The Composition, Pore Structure Characterization and Deformation Mechanism of Coal-Bearing Shales from Tectonically Altered Coalfields in Eastern China. *Fuel* 234, 626–642. doi:10.1016/j.fuel.2018.06.116

Li, X., Jiang, Z., Jiang, S., Li, Z., Song, Y., Jiang, H., et al. (2020). Characteristics of Matrix-Related Pores Associated with Various Lithofacies of marine Shales inside of Guizhong Basin, South China. *J. Pet. Sci. Eng.* 185, 106671–106716. doi:10.1016/j.petrol.2019.106671

Liu, J., Lu, D., and Li, P. (2019). Nano-scale Dual-Pore-Shape Structure and Fractal Characteristics of Transitional Facies Shale Matrix. *J. Nat. Gas Sci. Eng.* 68, 102907–102913. doi:10.1016/j.jngse.2019.102907

Liu, R., Hao, F., Engelder, T., Shu, Z., Yi, J., Xu, S., et al. (2019). Stress Memory Extracted from Shale in the Vicinity of a Fault Zone: Implications for Shale-Gas Retention. *Mar. Pet. Geology.* 102, 340–349. doi:10.1016/j.marpetgeo.2018.12.047

Liu, R., Jiang, D., Zheng, J., Hao, F., Jing, C., Liu, H., et al. (2021a). Stress Heterogeneity in the Changning Shale-Gas Field, Southern Sichuan Basin: Implications for a Hydraulic Fracturing Strategy. *Mar. Pet. Geology.* 132, 105218. doi:10.1016/j.marpetgeo.2021.105218

Liu, R., Wen, T., Amalberti, J., Zheng, J., Hao, F., and Jiang, D. (2021b). The Dichotomy in noble Gas Signatures Linked to Tectonic Deformation in Wufeng-Longmaxi Shale, Sichuan Basin. *Chem. Geology.* 581, 120412. doi:10.1016/j.chemgeo.2021.120412

Liu, R., Zheng, J., Hao, F., Nie, Z., Heng, D., Tan, X., et al. (2020). Variation in Pore Systems with Tectonic Stress in the Overthrust Wufeng-Longmaxi Shale of the Southern Sichuan Basin, China. *J. Nat. Gas Sci. Eng.* 83, 103617. doi:10.1016/j.jngse.2020.103617

Liu, S., Wu, C., Li, T., and Wang, H. (2018). Multiple Geochemical Proxies Controlling the Organic Matter Accumulation of the marine-continental Transitional Shale: A Case Study of the Upper Permian Longtan Formation, Western Guizhou, China. *J. Nat. Gas Sci. Eng.* 56, 152–165. doi:10.1016/j.jngse.2018.06.007

Liu, X., Xiong, J., and Liang, L. (2015). Investigation of Pore Structure and Fractal Characteristics of Organic-Rich Yanchang Formation Shale in central China by Nitrogen Adsorption/desorption Analysis. *J. Nat. Gas Sci. Eng.* 22, 62–72. doi:10.1016/j.jngse.2014.11.020

Loucks, R. G., Reed, R. M., Ruppel, S. C., and Jarvie, D. M. (2009). Morphology, Genesis, and Distribution of Nanometer-Scale Pores in Siliceous Mudstones of the Mississippian Barnett Shale. *J. Sediment. Res.* 79 (12), 848–861. doi:10.2110/jsr.2009.092

Luo, W., Hou, M., Liu, X., Huang, S., Chao, H., Zhang, R., et al. (2018). Geological and Geochemical Characteristics of marine-continental Transitional Shale from the Upper Permian Longtan Formation, Northwestern Guizhou, China. *Mar. Pet. Geology.* 89, 58–67. doi:10.1016/j.marpetgeo.2017.06.029

Luo, X., Zhao, Z., Hou, L., Lin, S., Sun, F., Zhang, L., et al. (2021). Experimental Methods for the Quantitative Assessment of the Volume Fraction of Movable Shale Oil: A Case Study in the Jimsar Sag, Junggar Basin, China. *Front. Earth Sci.* 9, 1–11. doi:10.3389/feart.2021.663574

Mendhe, V. A., Mishra, S., Varma, A. K., Kamble, A. D., Bannerjee, M., and Sutay, T. (2017). Gas Reservoir Characteristics of the Lower Gondwana Shales in Raniganj Basin of Eastern India. *J. Pet. Sci. Eng.* 149, 649–664. doi:10.1016/j.petrol.2016.11.008

Milliken, K. L., Rudnicki, M., Awwiller, D. N., and Zhang, T. (2013). Organic Matter-Hosted Pore System, Marcellus Formation (Devonian), Pennsylvania. *Bulletin* 97 (2), 177–200. doi:10.1306/07231212048

Nelson, P. H. (2009). Pore-throat Sizes in Sandstones, Tight Sandstones, and Shales. *Bulletin* 93 (3), 329–340. doi:10.1306/10240808059

Pan, J., Peng, C., Wan, X., Zheng, D., Lv, R., and Wang, K. (2017). Pore Structure Characteristics of Coal-Bearing Organic Shale in Yuzhou coalfield, China Using Low Pressure N 2 Adsorption and FESEM Methods. *J. Pet. Sci. Eng.* 153, 234–243. doi:10.1016/j.petrol.2017.03.043

Peltonen, C., Marcussen, Ø., Bjørlykke, K., and Jahren, J. (2009). Clay mineral Diagenesis and Quartz Cementation in Mudstones: The Effects of Smectite to Illite Reaction on Rock Properties. *Mar. Pet. Geology.* 26 (6), 887–898. doi:10.1016/j.marpetgeo.2008.01.021

Phaye, D. K., Bhattacharya, B., and Chakrabarty, S. (2021). Heterogeneity Characterization from Sequence Stratigraphic Analysis of Paleocene-Early Eocene Cambay Shale Formation in Jambusar-Broach Area, Cambay Basin, India. *Mar. Pet. Geology.* 128, 104986–105105. doi:10.1016/j.marpetgeo.2021.104986

Qin, L., Li, S., Zhai, C., Lin, H., Zhao, P., Shi, Y., et al. (2020). Changes in the Pore Structure of lignite after Repeated Cycles of Liquid Nitrogen Freezing as Determined by Nitrogen Adsorption and Mercury Intrusion. *Fuel* 267, 117214–117224. doi:10.1016/j.fuel.2020.117214

Rouquerol, J., Avnir, D., Fairbridge, C. W., Everett, D. H., Haynes, J. M., Pernicone, N., et al. (1994). Recommendations for the Characterization of Porous Solids (Technical Report). *Pure Appl. Chem.* 66 (8), 1739–1758. doi:10.1351/pac199466081739

Song, L., Martin, K., Carr, T. R., and Ghahfarokhi, P. K. (2019). Porosity and Storage Capacity of Middle Devonian Shale: A Function of thermal Maturity, Total Organic Carbon, and clay Content. *Fuel* 241, 1036–1044. doi:10.1016/j.fuel.2018.12.106

Sun, C., Nie, H., Dang, W., Chen, Q., Zhang, G., Li, W., et al. (2021). Shale Gas Exploration and Development in China: Current Status, Geological Challenges, and Future Directions. *Energy Fuels* 35 (8), 6359–6379. doi:10.1021/acs.energyfuels.0c04131

Sun, M., Yu, B., Hu, Q., Yang, R., Zhang, Y., Li, B., et al. (2018). Pore Structure Characterization of Organic-Rich Niutitang Shale from China: Small Angle Neutron Scattering (SANS) Study. *Int. J. Coal Geology.* 186, 115–125. doi:10.1016/j.coal.2017.12.006

Sun, Z., Wang, Y., Wei, Z., Zhang, M., Wang, G., and Wang, Z. (2017). Characteristics and Origin of Desorption Gas of the Permian Shanxi Formation Shale in the Ordos Basin, China. *Energy Exploration & Exploitation* 35 (6), 792–806. doi:10.1177/0144598717723564

Tang, S., Zhang, J., Elsworth, D., Tang, X., Li, Z., Du, X., et al. (2016). Lithofacies and Pore Characterization of the Lower Permian Shanxi and Taiyuan Shales in the Southern North China Basin. *J. Nat. Gas Sci. Eng.* 36, 644–661. doi:10.1016/j.jngse.2016.11.013

Tang, S., Zhang, J., and Zhu, W. (2021). Quantitative Evaluation of Organic Richness from Correlation of Well Logs and Geochemical Data: a Case Study of the Lower Permian Taiyuan Shales in the Southern North China Basin. *Front. Earth Sci.* 15 (2), 360–377. doi:10.1007/s11707-021-0930-9

Tang, X., Jiang, S., Jiang, Z., Li, Z., He, Z., Long, S., et al. (2019). Heterogeneity of Paleozoic Wufeng-Longmaxi Formation Shale and its Effects on the Shale Gas Accumulation in the Upper Yangtze Region, China. *Fuel* 239, 387–402. doi:10.1016/j.fuel.2018.11.022

Tang, X., Jiang, Z., Jiang, S., and Li, Z. (2016). Heterogeneous Nanoporosity of the Silurian Longmaxi Formation Shale Gas Reservoir in the Sichuan Basin Using the QEMSCAN, FIB-SEM, and Nano-CT Methods. *Mar. Pet. Geology.* 78, 99–109. doi:10.1016/j.marpetgeo.2016.09.010

Wang, G.-C., Sun, M.-Z., Gao, S.-F., and Tang, L. (2018). The Origin, Type and Hydrocarbon Generation Potential of Organic Matter in a marine-continental Transitional Facies Shale Succession (Qaidam Basin, China). *Sci. Rep.* 8 (1), 568–582. doi:10.1038/s41598-018-25051-1

Wang, G., Ju, Y., Yan, Z., and Li, Q. (2015). Pore Structure Characteristics of Coal-Bearing Shale Using Fluid Invasion Methods: A Case Study in the Huainan-Huaibei Coalfield in China. *Mar. Pet. Geology.* 62, 1–13. doi:10.1016/j.marpetgeo.2015.01.001

Wang, H., Liang, J., Li, X., Ji, X., Zhang, Q., and Huang, R. (2017). Analysis of the Geological Conditions for Shale Gas Accumulation: Two Different Carboniferous Marine-Continental Transitional Facies in the Bayanhot Basin, China. *Energy Fuels* 31 (11), 11515–11522. doi:10.1021/acs.energyfuels.7b00611

Wang, Y., Liu, L., Zheng, S., Luo, Z., Sheng, Y., and Wang, X. (2019). Full-scale Pore Structure and its Controlling Factors of the Wufeng-Longmaxi Shale, Southern Sichuan Basin, China: Implications for Pore Evolution of Highly Overmature marine Shale. *J. Nat. Gas Sci. Eng.* 67, 134–146. doi:10.1016/j.jngse.2019.04.020

Xi, Z., Tang, S., Wang, J., Yang, G., and Li, L. (2018). Formation and Development of Pore Structure in marine-continental Transitional Shale from Northern China across a Maturation Gradient: Insights from Gas Adsorption and Mercury Intrusion. *Int. J. Coal Geology.* 200, 87–102. doi:10.1016/j.coal.2018.10.005

Xi, Z., Tang, S., Zhang, S., and Li, J. (2017a). Nano-Scale Pore Structure of Marine-Continental Transitional Shale from Liulin Area, the Eastern Margin of Ordos Basin, China. *J. Nanosci. Nanotechnol.* 17 (9), 6109–6123. doi:10.1166/jnn.2017.14501

Xi, Z., Tang, S., Zhang, S., and Sun, K. (2017b). Pore Structure Characteristics of Marine-Continental Transitional Shale: A Case Study in the Qinshui Basin, China. *Energy Fuels* 31 (8), 7854–7866. doi:10.1021/acs.energyfuels.7b00911

Xie, W., Wang, M., Wang, H., Ma, R., and Duan, H. (2021). Diagenesis of Shale and its Control on Pore Structure, a Case Study from Typical marine, Transitional and continental Shales. *Front. Earth Sci.* 15 (2), 378–394. doi:10.1007/s11707-021-0922-9

Yan, G., Qin, Z., Marsh, S., Grebby, S., Mou, Y., Song, L., et al. (2021). Nanopore Size Distribution Heterogeneity of Organic-Rich Shale Reservoirs Using Multifractal Analysis and its Influence on Porosity-Permeability Variation. *Energy Fuels* 35 (17), 13700–13711. doi:10.1021/acs.energyfuels.1c01654

Yan, G., Wei, C., Song, Y., and Zhang, J. (2017). Pore Characteristics of Organic-Rich Shale in the Carboniferous-Permian Coal-Bearing Strata in Qinshui Basin. *Energy Exploration & Exploitation* 35 (5), 645–662. doi:10.1177/0144598717709668

Yang, C., Zhang, J., Tang, X., Ding, J., Zhao, Q., Dang, W., et al. (2017a). Comparative Study on Micro-pore Structure of marine, Terrestrial, and Transitional Shales in Key Areas, China. *Int. J. Coal Geology.* 171, 76–92. doi:10.1016/j.coal.2016.12.001

Yang, C., Zhang, J., Wang, X., Tang, X., Chen, Y., Jiang, L., et al. (2017b). Nanoscale Pore Structure and Fractal Characteristics of a marine-continental Transitional Shale: A Case Study from the Lower Permian Shanxi Shale in the southeastern Ordos Basin, China. *Mar. Pet. Geology.* 88, 54–68. doi:10.1016/j.marpetgeo.2017.07.021

Yang, R., He, S., Hu, Q., Sun, M., Hu, D., and Yi, J. (2017). Applying SANS Technique to Characterize Nano-Scale Pore Structure of Longmaxi Shale, Sichuan Basin (China). *Fuel* 197, 91–99. doi:10.1016/j.fuel.2017.02.005

Yu, K., Ju, Y., and Shao, C. (2020). Structure Characteristics and Evolution Mechanism of Nanopore in Transitional Coal-Bearing Shale. *J. Pet. Sci. Eng.* 184, 106545–106614. doi:10.1016/j.petrol.2019.106545

Zhang, J., Li, X., Wei, Q., Sun, K., Zhang, G., and Wang, F. (2017). Characterization of Full-Sized Pore Structure and Fractal Characteristics of Marine-Continental Transitional Longtan Formation Shale of Sichuan Basin, South China. *Energy Fuels* 31, 10490–10504. doi:10.1021/acs.energyfuels.7b01456

Zhang J., J., Li, X., Xiaoyan, Z., Zhao, G., Zhou, B., Li, J., et al. (2019). Characterization of the Full-Sized Pore Structure of Coal-Bearing Shales and its Effect on Shale Gas Content. *Energy Fuels* 33 (3), 1969–1982. doi:10.1021/acs.energyfuels.8b04135

Zhang, L., Karthikeyan, R., Bai, Z., and Srinivasan, R. (2017). Analysis of Streamflow Responses to Climate Variability and Land Use Change in the Loess Plateau Region of China. *Catena* 154, 1–11. doi:10.1016/j.catena.2017.02.012

Zhang, L., Li, B., Jiang, S., Xiao, D., Lu, S., Zhang, Y., et al. (2018). Heterogeneity Characterization of the Lower Silurian Longmaxi marine Shale in the Pengshui Area, South China. *Int. J. Coal Geology.* 195, 250–266. doi:10.1016/j.coal.2018.05.015

Zhang, M., and Fu, X. (2018). Study of the Characteristics of Marine-Terrigenous Facies Shale from the Permo-Carboniferous System in the Guxian Block, Southwest Qinshui Basin. *Energy Fuels* 32 (2), 1096–1109. doi:10.1021/acs.energyfuels.7b02556

Zhang M., M., Fu, X., Zhang, Q., and Cheng, W. (2019). Research on the Organic Geochemical and mineral Composition Properties and its Influence on Pore Structure of Coal-Measure Shales in Yushe-Wuxiang Block, South Central Qinshui Basin, China. *J. Pet. Sci. Eng.* 173, 1065–1079. doi:10.1016/j.petrol.2018.10.079

Conflict of Interest: Author ZY is employed by Lanyan Coalbed Methane Engineering Research Co. Ltd. Shanxi Gas Group.

The remaining authors declare that the research was conducted in the absence of any commercial or financial relationships that could be construed as a potential conflict of interest.

Publisher's Note: All claims expressed in this article are solely those of the authors and do not necessarily represent those of their affiliated organizations, or those of the publisher, the editors and the reviewers. Any product that may be evaluated in this article, or claim that may be made by its manufacturer, is not guaranteed orendorsed by the publisher.